ELSEVIER

Contents lists available at ScienceDirect

Pharmacological Research - Natural Products

journal homepage: www.sciencedirect.com/journal/prenap

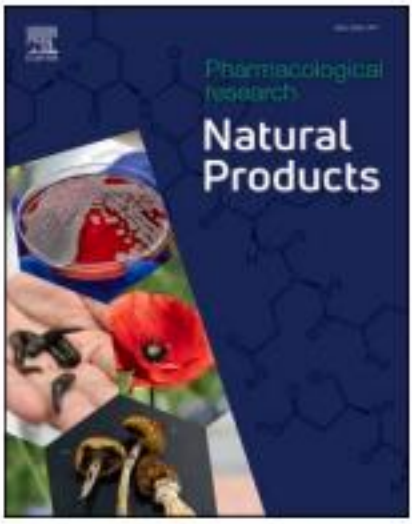

Computational approach by molecular docking and molecular dynamics of compounds from two Congolese medicinal plants as potent antisickling agents

Benjamin Z. Gbolo a,b,*,1, Wafa Ali Eltayb c,2,3, K.N. Ngbolua a,4, Samah Shabana d,5, Irène Semay e,6, Hamed I. Hamouda f,7, P. Gerbaux e,8, Mohamed Mohsen g,9, Emmanuel M. Kitete h,10, Pius T. Mpiana h,11, Xiling Wang i,12, Pierre Duez b,13, Mohnad Abdalla j,**,14

ARTICLE INFO

Keywords: Molecular docking Molecular dynamics simulation Pharmacokinetic study Hb S polymerization, OSAR, Sickle cell disease

ABSTRACT

Background: Sickle cell disease is a genetic disorder caused by hemoglobin S, and its treatment remains challenging. Compounds that penetrate erythrocytes to stabilize hemoglobin S are potential therapeutic agents. This study evaluated the *in silico* antisickling activity of 13 isolated flavonoids from Justicia secunda and Moringa oleifera using molecular docking and dynamics.

Methods: Deoxyhemoglobin (3WCU) and human bisphosphoglycerate mutase (3NFY) were used as receptor proteins. Flavonoids were identified via LC-MS/MS in positive and negative modes. Frontier molecular orbital

E-mail addresses: benjamin.gbolo@unikin.ac.cd (B.Z. Gbolo), wafa.ali.11338@gmail.com (W.A. Eltayb), jpngbolua@unikin.ac.cd (K.N. Ngbolua), sshabana@163. com (S. Shabana), Irene.SEMAY@umons.ac.be (I. Semay), hamed@qibebt.ac.cn (H.I. Hamouda), Pascal.GERBAUX@umons.ac.be (P. Gerbaux), m.mohsen@azhar. edu.eg (M. Mohsen), emmanuel.kitete@gmail.com (E.M. Kitete), pt.mpiana@unikin.ac.cd (P.T. Mpiana), wangxl@qibebt.ac.cn (X. Wang), pierre.DUEZ@umons. ac.be (P. Duez), mohnadab-dalla200@gmail.com (M. Abdalla).

https://doi.org/10.1016/j.prenap.2026.100516

a Department of Biology, Faculty of Sciences, University of Kinshasa, P.O. Box 190, Kinshasa XI, Democratic Republic of the Congo

b Unit of Therapeutic Chemistry and Pharmacognosy, Faculty of Medicine and Pharmacy, University of Mons (UMONS), Mons 7000, Belgium

<sup>c Biotechnology Department, Faculty of Science and Technology, Shendi University, Shendi, Nher Anile, Sudan

d Department of Biochemistry and Molecular Biology, College of Marine Life Sciences, Ocean University of China, Qingdao 266003, PR China

e Organic Synthesis and Mass Spectrometry Laboratory(S2MOs), Research Institute for Biosciences, University of Mons (UMONS), Mons 7000, Belgium

f Processes Development Department, EPRI, Nasr City, Cairo 11727, Egypt

<sup>g Fish Production Department, Faculty of Agriculture, Al-Azhar University, Nasr City, Cairo 11884, Egypt

h Department of Chemistry, Faculty of Sciences, University of Kinshasa, P.O. Box 190, Kinshasa XI, Democratic Republic of the Congo

<sup>i CAS Key Laboratory of Biofuels and Shandong Provincial Key Laboratory of Synthetic Biology, Qingdao Institute of Bioenergy and Bioprocess Technology Chinese Academy of Sciences, Qingdao, Shandong 266101, China

<sup>j Pediatric Research Institute, Children’s Hospital Affiliated to Shandong University, Jinan 250022, China

* Corresponding author at: Department of Biology, Faculty of Sciences, University of Kinshasa, P.O. Box 190, Kinshasa XI, Democratic Republic of the Congo.

** Corresponding author.

<sup>1 https://orcid.org/0000-0001-8305-5901

<sup>2 Contributed equally to this work

<sup>3 https://orcid.org/0000-0002-3981-201X

<sup>4 https://orcid.org/0000-0002-0066-8153

<sup>5 https://orcid.org/0000-0001-5624-8089

6 https://orcid.org/0000-0002-4197-0316

<sup>7 https://orcid.org/0000-0002-5980-0796

8 https://orcid.org/0000-0001-5114-4352

<sup>9 https://orcid.org/0000-0003-1258-8764

<sup>10 https://orcid.org/0002-3195-286X

11 https://orcid.org/0000-0002-8590-6017

12 https://orcid.org/0000-0002-2805-8146

13 https://orcid.org/0000-0002-0484-1478

14 https://orcid.org/0000-0002-1682-5547

(FMO) analysis, QSAR studies, ADMET profiling, and molecular dynamics simulations (MD) were conducted to assess reactivity, stability, and drug-likeness.

Results: Four compounds (C_3, C_9, C_11, C_12) showed the highest docking activity, with C_11 and C_12 emerging as top ligands. FMO analysis indicated HOMO energies (–5.496 to –5.917 eV) and LUMO energies (–1.139 to –1.468 eV). Water solubility, GI absorption, BBB permeability, and CYP interactions were predicted, with all compounds classified as soluble but low GI absorption and non-BBB permeant. Drug-likeness evaluation showed multiple violations, typical for large flavonoids, while bioavailability scores were 0.17. Medicinal chemistry filters revealed minimal PAINS/Brenk alerts with synthetic accessibility ranging 3.82–7.42. Docking and hydrogen-bond analyses indicated that C_11 and C_12 interacted with key residues of 3WCU and 3NFY. MD simulations and ADMET profiles confirmed the stability and drug-like potential of C_11 and C_12 as promising *in silico* leads.

Conclusion: In silico analyses suggest that C_11 and C_12 are promising candidates for antisickling drug development, supported by binding affinity, molecular stability, hydrogen-bond interactions, and favorable quantum chemical, physico-chemical, and pharmacokinetic properties.

1. Introduction

Sickle cell disease (SCD) is among the most common and severe inherited genetic disorders worldwide. It results from a single point mutation in the β-globin chain of hemoglobin, where valine replaces glutamic acid at position six, decreasing hemoglobin solubility during deoxygenation [1–3]. This alteration triggers the sickling of red blood cells, leading to vascular obstruction, increased membrane fragility, and premature hemolysis, which together cause chronic hemolytic anemia and recurrent vaso-occlusive crises [4–6].

Multiple studies have highlighted modulatory factors that influence hemoglobin S (Hb S) polymerization, including 2,3-diphosphoglycerate (2,3-DPG) concentrations and red cell dehydration [5,7]. Elevated 2, 3-DPG reduces hemoglobin's oxygen affinity and thereby promotes polymerization [8–10], whereas dehydration increases intracellular Hb S levels, enhancing gelation and fiber formation [11]. Dehydration is largely driven by activation of the Gardos channel, which induces potassium loss followed by water efflux from the erythrocyte [12,13].

Current pharmacological approaches focus on identifying molecules capable of entering red blood cells, stabilizing Hb S, and disrupting fiber formation [10,14,15]. Inhibiting 2,3-DPG can delay polymerization, allowing more erythrocytes to circulate before fiber assembly occurs [3, 10,16]. Similarly, targeting the Gardos channel to prevent dehydration is considered a promising therapeutic strategy [3,7,17].

In this context, deoxyhemoglobin (PDB ID: 3WCU) and human bisphosphoglycerate mutase (PDB ID: 3NFY) were selected as molecular targets. Stable binding to deoxyhemoglobin suggests the ability of a compound to stabilize Hb S and impede polymer formation, whereas interaction with human BPGM reflects its potential to modulate the Rapoport–Luebering pathway responsible for generating 2,3-DPG, the primary factor lowering Hb S oxygen affinity [18].

Although previous studies have demonstrated antisickling activity in crude flavonoid extracts from the Congolese plants *Justicia secunda* and *Moringa oleifera* [19,20], the molecular basis of their protective effects remains insufficiently defined. This study uses molecular docking, molecular dynamics simulations, and ADMET analyses to clarify the mechanisms by which these flavonoids may act as inhibitors of Hb S polymerization.

2. Materials and methods

2.1. Preparation of the ligands

2.1.1. Flavonoid analysis by LC-MS/MS

The flavonoid-rich subfractions from *Justicia secunda* and *Moringa oleifera* were analyzed in both positive and negative ionization modes. Samples of the extracts from *J. secunda* (0.0586 g) and *M. oleifera* (0.0118 g) were diluted 1:100 in methanol prior to mass spectrometric analysis. For positive mode experiments, HPLC-MS and HPLC-MS/MS analyses were performed using a Waters Synapt G2-Si mass spectrometer equipped with an electrospray ionization source, coupled to a Waters Acquity UPLC H-Class system (Waters, Manchester, UK). Chromatographic separation was achieved on a Phenomenex Kinetex C18 EVO column (00F-4633-AN, 150 × 2.1 mm, 5 µm particle size) under reversed-phase conditions. A binary gradient elution was applied at a flow rate of 0.25 mL/min, with water containing 0.1 % formic acid as solvent A and methanol as solvent B. The column temperature was maintained at 40◦C. Mass spectrometry parameters were set as follows: capillary voltage 2.5 kV, cone voltage 40 V, source temperature 120◦C, and desolvation temperature 300 ◦C. For negative mode experiments, HPLC-MS and HPLC-MS/MS analyses were carried out using a Waters Q-ToF US mass spectrometer (electrospray ion source) coupled to a Waters Alliance 2695 HPLC system (Waters, Manchester, UK). The capillary voltage was set to 3.1 kV and the cone voltage to 30 V, while the remaining operational parameters, including source and desolvation temperatures, flow rate, column, and gradient conditions, were maintained as described for positive mode analyses. This dual-mode approach allowed comprehensive detection and identification of flavonoid constituents in both plant extracts.

2.1.2. Ligands selection

Thirteen flavonoids were selected and sketched in 2D using Chem-Draw software, from which their corresponding 3D structures were generated and saved in SDF format. The ligands were then subjected to geometric optimization using MGLTools version 1.5.7.

2.2. Choice of receptors

To validate the anti-sickling activity of the selected molecules, docking studies focused on two proteins that play central roles in HbS polymerization. The first, bisphosphoglycerate mutase (BPGM, PDB ID: 3NFY), catalyzes the conversion of 1,3-bisphospho-D-glycerate into 2,3 bisphospho-D-glycerate (2,3-BPG). In sickle cell erythrocytes, excess 2,3-BPG, along with sphingosine-1-phosphate (S1P), decreases hemoglobin's oxygen affinity, increasing the proportion of deoxyHbS available for polymerization. The second, deoxyhemoglobin (PDB ID: 3WCU), directly polymerizes, triggering red blood cell deformation and sickling. These targets were selected for their decisive contribution to SCD pathophysiology: HbS polymerization drives the structural distortion of erythrocytes, while BPGM regulates oxygen affinity and indirectly influences HbS stability [10,18]. Exploring how anti-sickling compounds interact with both proteins offers a dual therapeutic strategy—stabilizing HbS to limit polymerization while modulating 2,3-BPG levels to preserve hemoglobin's oxygen-binding capacity—thus addressing two critical molecular mechanisms underlying the clinical manifestations of sickle cell disease [10,18].

2.3. Preparation of the receptors

The three-dimensional crystal structures of human

Table 1 Binding affinity (kcal/mol) of receptors and ligands.

Deoxyhemoglobin (3wcu)	Heme (Control)Apigenin-7-Oglucosylglucosylrhamnoside (C_3)Kaempferid-7-O-dixyloside (C_11)	-12.2-10.5
		-10.1
	Apigenin-7-O- dixyloside (C_12)	-10.1
	Luteolin-7-O-glucosylrhamnoside(C_5)	-10
	Kaempferid-7-O xylosylrhamnoside (C_13)	-10
	Luteolin-7-O glucosylrhamnosylrhamnoside(C_4)	-9.8
	Kaempferid-7-O-xylosylglucoside(C_7)	-9.7
	Luteolin-7-O glucosylglucosylrhamnoside (C_2)	-9.6
	Luteolin-7-O- xylosylglucoside (C_8)	-9.6
	Luteolin-7-O- xylosylxyloside (C_9)	-9.6
	Luteolin-7-O- xylosylrhamnoside(C_10)	-9.6
	Disodium cromoglicate C_1(control)	-9.6
	Kaempferid-7-O-glucosylxyloside(C_6)	-9.5
	Apigenin-8-C- glucoside (C_14)	-9.5
HumanBiphosphoglycerate	Disodium cromoglicate C_1(control)	-10.6
Mutase (3nfy)	Kaempferid-7-O-dixyloside (C_11)	-10.5
	Apigenin-7-O- dixylosideC_12	-10.2
	Luteolin-7-O- xylosylxyloside (C_9)	-10.2
	Luteolin-7-O- xylosylrhamnoside(C_10)	-9.9
	Kaempferid-7-O-glucosylxyloside(C_6)	-9.4
	Luteolin-7-O- xylosylglucoside (C_8)	-8.9
	Kaempferid-7-O-xylosylglucoside(C_7)	-8.7
	Kaempferid-7-O xylosylrhamnoside (C_13)	-8.6
	Apigenin-8-C- glucoside (C_14)	-8.2
	Apigenin-7-O glucosylglucosylrhamnoside (C_3)	-8
	Luteolin-7-O-glucosylrhamnoside (C_5)	-7.9
	Luteolin-7-O glucosylglucosylrhamnoside (C_2)	-7.1
	Luteolin-7-Oglucosylrhamnosylrhamnoside	-6.1

bisphosphoglycerate mutase (BPGM) (PDB ID: 3NFY) and deoxyhemoglobin (PDB ID: 3WCU) were retrieved from the Protein Data Bank (https://www.rcsb.org). Visualization of the proteins and removal of crystallographic water molecules were carried out using Discovery Studio Visualizer 2000. Atomic vacancies and crystallographic inconsistencies were corrected by energy minimization with MGLTools version 1.5.7. Structural validation of both receptors was performed using Ramachandran plot analysis, a standard tool in structural bioinformatics for assessing stereochemical quality. This method evaluates the distribution of the φ (phi) and ψ (psi) dihedral angles of amino acid residues to identify sterically favorable conformations. Ramachandran plots for both receptors were generated via PROCHECK, embedded in the PDBsum server at EMBL-EBI (https://www.ebi.ac.uk/thornton-srv/ databases/pdbsum). According to accepted criteria, a structure is considered reliable when at least 90 % of its residues fall within favored regions. The optimized protein structures were then saved in pdbqf format for subsequent docking simulations.

2.4. QSAR analysis

The quantitative structure–activity relationship (QSAR) is an approach used to establish correlations between the structural properties of chemical compounds and their biological activities. This method allows the selection and prediction of compounds with potential desired activities. In this study, QSAR calculations were carried out using HyperChem Professional 8.0.3 software. The optimization of the selected compounds was achieved through the MM+ force field and the semi-empirical PM3 method, while the Fletcher–Reeves conjugate gradient algorithm was employed to minimize the molecular energy. Furthermore, several molecular descriptors were computed for all compounds, including molecular mass, volume, surface area, total energy, free energy, hydration energy, refractive index, RMS gradient, and polarizability.

2.5. Molecular docking

The orientations and conformations of the selected flavonoids with their targets—deoxyhemoglobin (PDB ID: 3WCU) and human bisphosphoglycerate mutase (PDB ID: 3NFY)—were determined using Auto-Dock Vina (v.4, The Scripps Research Institute, La Jolla, CA, USA). A blind docking approach was employed, allowing ligands to explore the entire protein surface without restriction to predefined binding pockets. This strategy facilitated the identification of the most energetically favorable ligand poses within protein cavities. Active sites were defined based on the crystallographic ligands of 3WCU and 3NFY, with docking grids centered on the respective proteins. AutoDock Vina, a gradientbased stochastic global optimization technique that combines Monte Carlo sampling with an iterated local search process, was used for docking runs. While the protein structures were kept rigid during the docking process, ligands were handled as completely flexible in this workflow [21]. The most favorable conformations were selected according to their lowest binding energy values. Docking outcomes were validated using PyRx and Discovery Studio Visualizer (BIOVIA, 2019) to characterize polar and hydrophobic interactions with key amino acid residues. Ligands showing stable interactions in the binding regions of 3WCU and 3NFY were identified as potential antisickling agents, capable of interfering with HbS polymerization and 2,3-BPG activity. To ensure methodological reliability, an internal validation was performed by re-docking crystallographic ligands into their original binding sites. The resulting RMSD values remained consistently below 2.0 Å, confirming both the accuracy and reproducibility of the docking protocol [22–26].

2.6. Molecular dynamics simulation

Following the completion of all docking procedures and calculations, only two compounds—kaempferol-7-O-dixyloside (C-11) and apigenin-7-O-dixyloside (C-12)—exhibited the highest binding affinities to the target proteins. These compounds were therefore selected as the best ligands for subsequent molecular dynamics (MD) simulations.

Molecular dynamics (MD) simulations were conducted using Desmond (version 2019–4, Schrodinger ¨ LLC) to evaluate the stability and conformational behavior of the protein–ligand complexes. Structural preparation was performed in Maestro using the Protein Preparation Wizard, including addition of hydrogen atoms, optimization of hydrogen-bonding networks, minimization of steric clashes, and reconstruction of missing side chains or residues when necessary. System setup was carried out using the System Builder module.

Each complex was embedded in an orthorhombic simulation box with a 12 Å buffer, solvated with the TIP3P water model, and neutralized with 0.15 M NaCl to mimic physiological ionic strength. The OPLS_2005 force field was applied to all components. Following system construction, an initial energy minimization and default Desmond equilibration protocol were performed to relax solvent and remove

Fig. 1. 2D chemical structures of the most active plant based compounds (C_3, C_9, C_11, C_12) extracted from *Justicia secunda* and *Moringa oleifera*.

Table 2 Computed quantum chemical parameters for the compounds.

Compound	LUMO (eV)	HOMO (eV)	ΔE (eV)	χ Pauling	η (eV)	σ	μ (eV)	S	ω (ev)
C_1	-1.68925	-5.41316102	3.72391115	-0.1305	1.8619663	14.61441	3.55119472	7.307206	3.38651141
C_3	-1.13996115	-5.51012414	4.37016299	-0.12219	2.1850743	12.45326	3.32504089	6.22663	2.52986977
C-9	-1.46890969	-5.78442724	4.31551754	-0.13328	2.1577540	612.61095	3.6266791	6.305475	3.04778408
C_11	-1.30003882	-5.49623588	4.19619706	-0.12488	2.0981067	112.96955	3.39813067	6.484773	2.75186025
C_12	-1.44949274	-5.91756011	4.46806738	-0.13537	2.2340275	812.18038	3.68352369	6.090192	3.03673625

(Legend: electronegativity (χ), Hardness (η), chemical potential (μ = − χ), softness (S), electrophilicity (ω) in eV)

unfavorable contacts.

Production MD simulations were performed for 100 ns under NPT ensemble conditions (310 K, 1 atm). Temperature and pressure were regulated using the Nos´e–Hoover thermostat and the Martyna–Tobias–Klein (MTK) barostat, respectively. Integration of equations of motion was carried out with a 2 fs time-step, with all bonds to hydrogen atoms constrained to enable stable long-timescale sampling. To ensure robustness and reproducibility, three independent replicates were executed with different random seeds. Trajectories were recorded every 100 ps, resulting in approximately 1000 frames per run.

Post-simulation analyses included root mean square deviation (RMSD) and root mean square fluctuation (RMSF) to assess structural stability and residue flexibility. Additionally, radius of gyration (rGyr) calculations were performed to examine ligand conformational dynamics, compactness, and flexibility under simulated physiological conditions. These metrics collectively enabled a detailed evaluation of complex stability and dynamic behavior over the simulated timescale [23–25].

2.7. Calculation of the binding free energy

The Molecular Mechanics Generalized Born Surface Area (MM-GBSA) method was employed to calculate the binding free energies of the ligands with their respective target proteins. Binding free energy estimations were performed using the Prime module of Schrodinger. ¨ After 100 ns of molecular dynamics simulation, the MM-GBSA method was applied to predict the thermodynamic stability and binding affinity of each protein–ligand complex.

3. Results and discussion

3.1. Ramachandran plots

The Ramachandran plot analysis of the 3NFY structure (Fig. S1) indicates that 98.2 % of residues are located in favored regions, 1.4 % in allowed regions, and only 0.4 % in disallowed regions. These results exceed the commonly accepted threshold of 90 % of residues in favored regions, confirming that the model adheres well to the stereochemical and conformational constraints of natural proteins and supporting the reliability of the predicted structure. Evaluation of the 3WCU protein structure (Fig. S2) shows that 87.7 % of residues (excluding glycines and prolines) occupy the most favored regions of the Ramachandran diagram,

12.1 % fall within additionally allowed regions, and 0.2 % are in generously allowed regions. No residues were found in disallowed regions, indicating good stereochemical consistency. Although the percentage of residues in the most favored regions is slightly below the 90 % threshold generally expected for high-resolution structures, it remains within an acceptable margin. Regarding the G-factors, the average value of 0.08, close to zero, reflects satisfactory overall geometry, despite minor deviations in the φ–ψ and χ1–χ2 distributions. Collectively, these

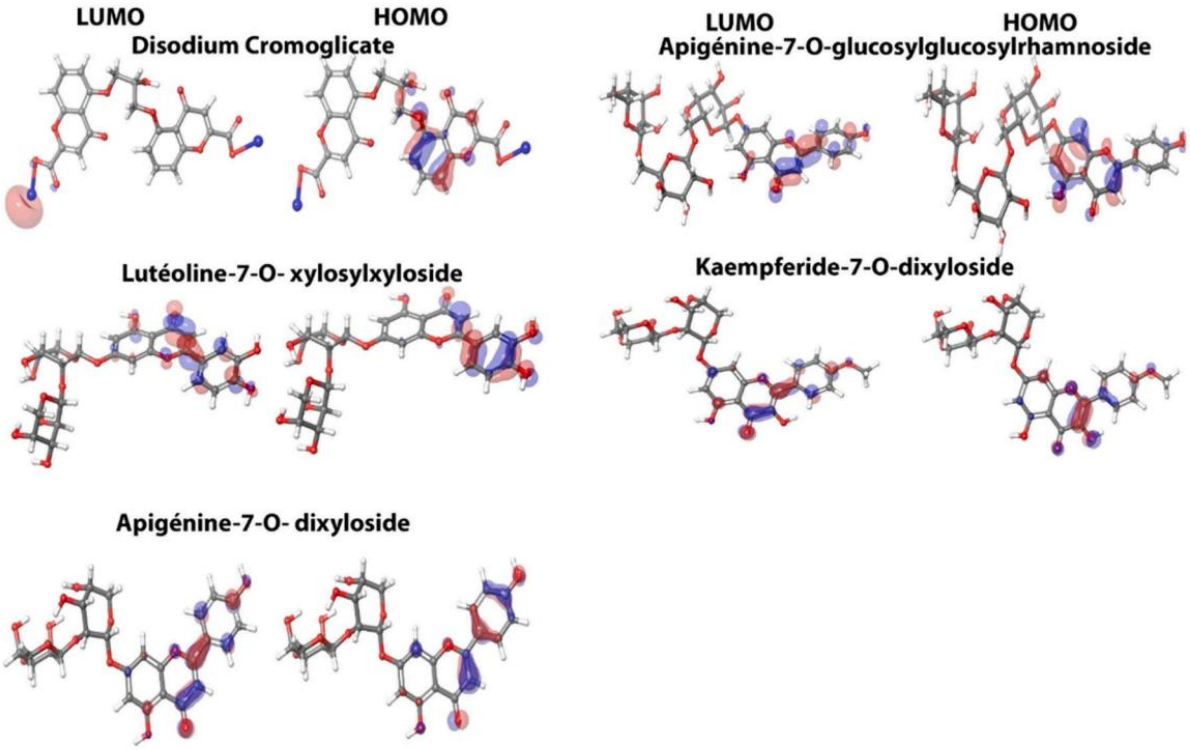

Fig. 2. HOMO and LUMO orbital shapes for C_1, C_3, C_9, C_11, and C_12, with a color scale (red for high electron density, blue for low) and labels for energy levels (eV) from Table 2.

Table 3 QSAR rating for optimized compounds.

Function	Compound 1	Compound 3	Compound 9	Compound 11	Compound 12
Surface area (Approx) (Å2)	618.64	775.42	572.59	615.17	567.55
Surface area (Grid) (Å2)	748.40	994.60	767.89	802.35	760.54
Volume (Å3)	1245.32	1806.49	1351.08	1406.14	1333.43
Hydration energy (Kcal/mole)	-23.76	-47.17	-40.60	-34.46	-34.36
Log P	9.32	1.36	2.36	2.30	2.54
Refractivity (Å3)	40.03	112.64	71.23	76.27	69.84
Polarizability (Å3)	42.75	66.89	49.80	51.64	49.17
Mass (amu)	512.34	740.67	550.47	564.50	534.47
Total energy (kcal/mol)	9.92102	36.8145	25.7372	28.4642	25.7649
Dipole Moment (Debye)	1.489	6.171	3.938	3.409	2.645
RMS Gradient (kcal/ Å mol)	0.09479	0.09863	0.09885	0.0961	0.09463

analyses suggest that the 3WCU model is of good structural quality, although targeted adjustments in certain regions could further optimize the model to fully meet high-resolution standards.

3.2. Binding affinity and Gibbs free energy of complexes

Table 1 gives the Gibbs free energy values of the complexes formed between the ligands and the two receptors.

As shown in Table 1, the selected compounds form thermodynamically stable complexes with both receptors ($\Delta G < 0$). For the complexes formed with 3WCU, eleven out of the thirteen flavonoids exhibit greater stability than the positive control (C_1). In contrast, for 3NFY, only the complex with C_11 shows a binding energy comparable to that of the positive control. These findings indicate that the flavonoids from the two Congolese plants potentially inhibit both the polymerization of deoxyhemoglobin S into tactoids and the activity of 2,3-bisphosphoglycerate mutase. Specifically, 3WCU (deoxyHb) was used to evaluate the stabilization of Hb S, while 3NFY (BPGM) was targeted to inhibit 2,3-DPG production—both mechanisms being critical in the pathophysiology of sickle cell disease [10,18].

In total, four compounds, along with sodium cromoglicate (Fig. 1),

were selected for further analysis.

3.3. Frontier molecular orbitals (FMOs) approach

The main chemical quantum parameters of the selected compounds are presented in Table 2.

The overall reactivity of the studied compounds was analyzed in terms of the energies of the highest occupied molecular orbital (HOMO) and lowest unoccupied molecular orbital (LUMO), the HOMO–LUMO energy gap (ΔE), and additional chemical reactivity descriptors. The ΔE values provide insights into the chemical reactivity and stability of the molecules [23,27].

The negative values obtained for EHOMO and ELUMO for all compounds confirm their intrinsic stability, while a smaller ΔE indicates a higher potential for charge transfer interactions. Consequently, a molecule with a large ΔE is expected to exhibit high stability but low chemical reactivity, whereas a smaller ΔE corresponds to increased reactivity [23,27]. In this study, the calculated stability of the compounds follows the order C_12 > C_3 > C_9 > C_11 > C_1, whereas their chemical reactivity varies inversely as C_12 < C_3 < C_9 < C_11 < C_1. These results suggest that C_12 is the most stable compound, while C_1

Table 4a Hydrogen-bond parameters derived from docking of the 3NFY receptor with the best ligands.

Ligand	Receptor	Interaction	Distance (Å)
	ARG_10	H-acceptor	2.88
	SER_24	H-acceptor	3.12
	ARG_62	H-acceptor	2.93
C_1	GLY_189	H-acceptor	3.33
	ARG_193	H-acceptor	2.81
	VAL_248	H-donor	2.78
C_9	GLU _13	H-donor	2.86
	ARG_21	H-donor	2.80
	GLU_89	H-donor	2.77
	ARG_100	H-acceptor	2.79
	ARG_116	H-acceptor	3.00
	ARG_193	H-acceptor	2.85
	ASN_209	H-donor	2.69
	THR_211	H-acceptor	3.28
	LEU_212	H-donor	3.33
	LEU_212	H-acceptor	2.63
	ASP_250	H-donor	2.56
	ARG_10	H-acceptor	2.85

Ligand	Receptor	Interaction	Distance (Å)
C_11	ARG_10	H-acceptor	3.01
	GLU_13	H-donor	2.64
	ASN_17	H-donor	2.73
	ASN_17	H-acceptor	2.82
	ASN_20	H-acceptor	2.86
	CYS_23	H-acceptor	3.04
	SER_24	H-acceptor	3.09
	ILE_208	H-donor	2.65
	ARG_10	H-acceptor	2.78
	ARG_10	H-acceptor	2.94
	ARG_10	H-acceptor	2.93
C_12	GLU_13	H-donor	2.69
	GLU_13	H-donor	2.64
	ASN_17	H-donor	2.65
	ASN_20	H-acceptor	2.83
	CYS_23	H-acceptor	2.99
	ARG_62	H-acceptor	2.98
	GLU_89	H-donor	3.19
	ASN_190	H-donor	2.68
	ASP_250	H-donor	2.55

Table 4b Hydrogen-bonds parameters derived from docking of 3WCU receptor with the best ligands.

Ligand	Receptor	Interaction	Distance (Å)
C_1	ARG_66	H-acceptor	2.95
	ARG 66	H-acceptor	2.85
	ARG_98	H-acceptor	2.93
	ARG_66	H-acceptor	2.85
C_3	HIS_95	H-acceptor	2.81
	ARG_98	H-acceptor	3.02
	ARG_98	H-acceptor	2.88
	ARG_66	H-acceptor	2.89
	ARG_66	H-acceptor	2.86
C_11	GLY_70	H-donor	2.78
	GLN_87	H-acceptor	2.86
	HIS_90	H-acceptor	3.01
	GLN_94	H-donor	2.78
	GLN_94	H-donor	2.91
	GLN_94	H-acceptor	2.82
	ARG_98	H-acceptor	2.89
C_12	ALA_43	H-donor	2.88
	ARG_66	H-acceptor	2.92
	GLY_70	H-donor	2.75
	MET_73	H-donor	3.21
	GLN_87	H-acceptor	2.89
	HIS_90	H-acceptor	3.05
	GLN_94	H-donor	2.73
	GLN_94	H-donor	2.89
	GLN_94	H-acceptor	2.92
	ARG_98	H-acceptor	2.93

exhibits the lowest stability.

Although the absolute values obtained for these two parameters are relatively low, the relative trends between molecules remain reliable and consistent, allowing for a relevant interpretation of their chemical reactivity and anti-sickling potential.

Further confirmation comes from additional chemical reactivity parameters (Table 2), including chemical potential (μ), electronegativity (χ), global softness (S), global hardness (η), and electrophilicity index (ω). A compound is generally more reactive when it exhibits higher chemical softness, whereas lower softness values indicate increased stability. In this study, all analyzed compounds display low S values, with C_12 showing the lowest, followed by C_3, C_9, C_11 (moderate), and C_1 (highest), corroborating the relative stabilities of the molecules. The electrophilicity index (ω) also provides insight into a compound's capacity to accept electrons, with positive values indicating such potential. The results indicate that all compounds are stable, with C_3 being the most stable due to its relatively low ω value compared to the others (Table 2).

HOMO and LUMO orbitals further reveal the electron donor and acceptor properties of a molecule, which are crucial for biological interactions with proteins. Interactions primarily occur between the HOMO of the ligand and the LUMO of the protein. Additionally, only residues present in both the protein's LUMO and a surface pocket participate actively in binding, defining the ligand's binding site (Fig. 2).

3.4. QSAR studies

The results of the QSAR of the selected molecules are shown in Table 3.

To anticipate the chemical reactivity and physicochemical properties of the selected compounds, QSAR analyses were performed. Key parameters, including refractivity, polarizability, molecular mass, molecular volume, hydration energy, surface area, total energy, free energy, and RMS gradient, were calculated for all compounds (Table 3). Additionally, the partition coefficient (log P) was estimated, as it provides critical insight into a compound's biological activity and its ability to permeate cell membranes [28–30]. Among the compounds studied, C_1, used as a reference, exhibited a log P value significantly higher than those of the other compounds, indicating a greater lipophilicity and potential for membrane permeability.

3.5. Molecular docking study

The results of this study indicate that the stability of the ligand–receptor complexes is primarily driven by weak molecular interactions, including Van der Waals forces, π–π stacking, and hydrogen bonds. The specific parameters of the hydrogen bonds formed between the receptors and the most active ligands, as determined from molecular docking, are summarized in Tables 4a and 4b and illustrated in Figs. 3 and 4.

The data presented in these two tables confirm the stability of the interactions between the different ligands and the receptors analyzed. Notably, several of the involved residues are capable of forming multiple hydrogen bonds simultaneously, thereby enhancing the stability, specificity, functional flexibility, and dynamic robustness of the protein. This is particularly the case for Asn, Gln, Asp, Glu, Ser, Thr, Tyr, His, Lys, and Arg (Figs. 3 and 4). Their side chains contain several donor and/or acceptor groups, allowing them to participate in more than one hydrogen bond simultaneously and thereby contribute to the stabilization of local structural motifs or dynamic interaction networks.

3.6. Molecular dynamics simulation

The overall stability was further investigated using RMSD and RMSF stability profile analysis.

The results of the RMSD and RMSF analyses are shown in Fig. 5

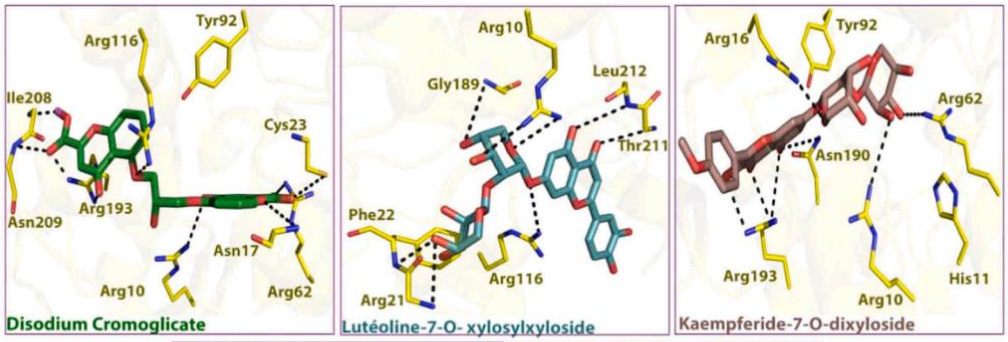

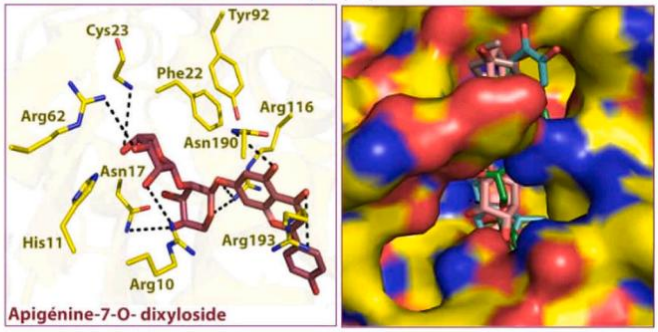

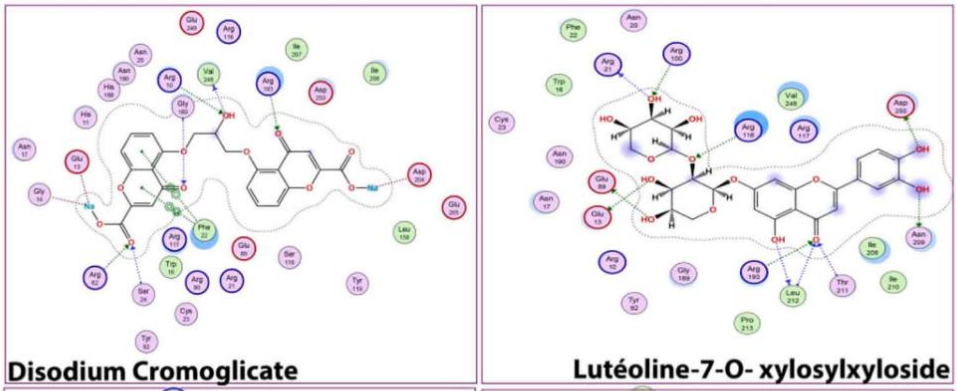

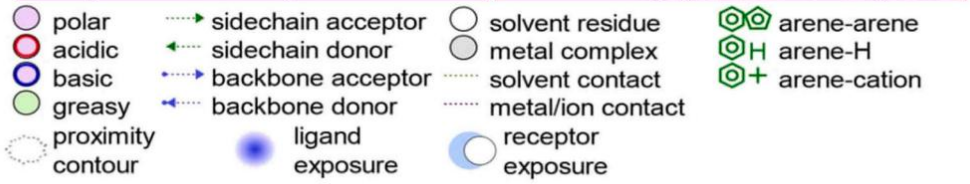

Human Bisphosphoglycerate Mutase PDB ID 3NFY

Fig. 3. Docking interactions of *C_9, C_11, and C_12* with human Bisphosphoglycerate Mutase (PDB ID: 3NFY*)*. 3D poses (A) and 2D interaction diagrams (B) show key hydrogen bonds, polar and hydrophobic contacts, and aromatic interactions. Residues such as Arg10, Arg62, Arg116, Asn17, Asn190, and Arg193 form recurrent interactions that contribute to complex stability.

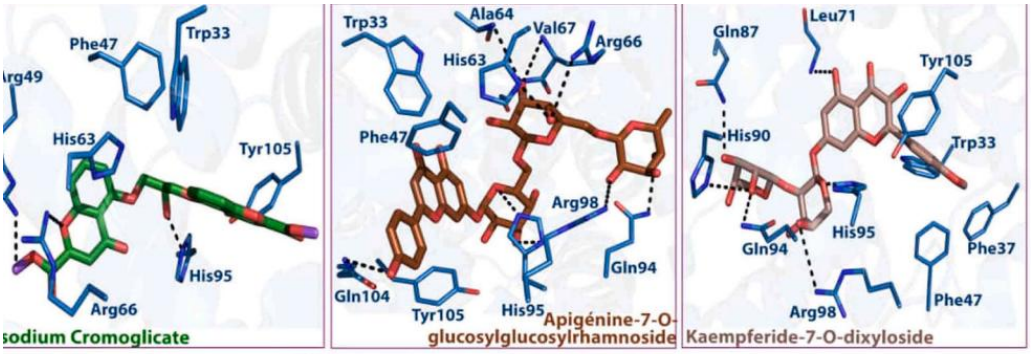
Phe47
Trp33
His63
Tyr105
His95
Arg66
odium Cromoglicate
Trp33
Ala64
Val67
Arg66
His63
Phe47
Arg98
Gln94
Gln104
Tyr105
His95
Apigénine-7-O-glucosylglucosylrhamnoside
Gln87
Leu71
Tyr105
His90
Trp33
Gln94
His95
Phe37
Arg98
Phe47
Kaempferide-7-O-dixyloside

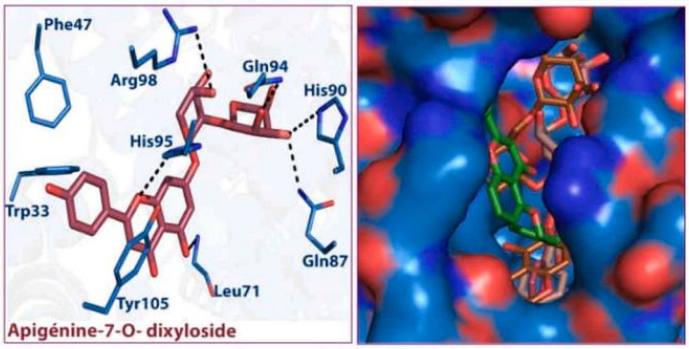
Phe47
Arg98
Gln94
His90
His95
Trp33
Gln87
Tyr105
Leu71
Apigénine-7-O- dixyloside

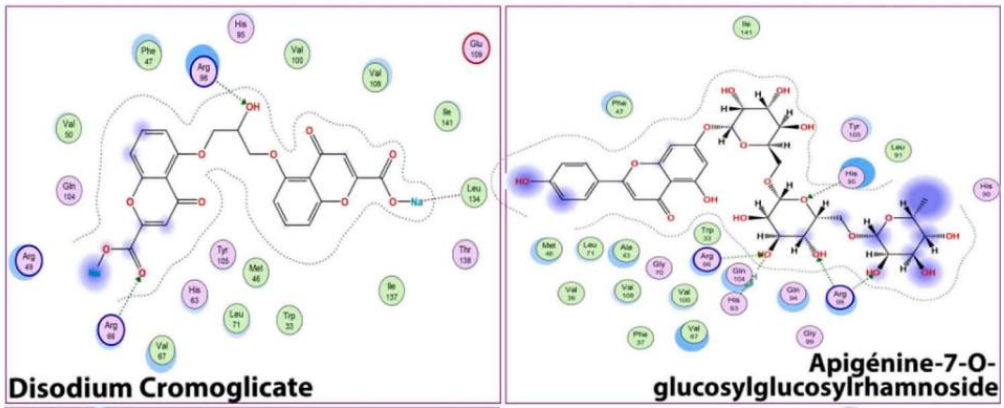
Disodium Cromoglicate
Apigénine-7-O-glucosylglucosylrhamnoside

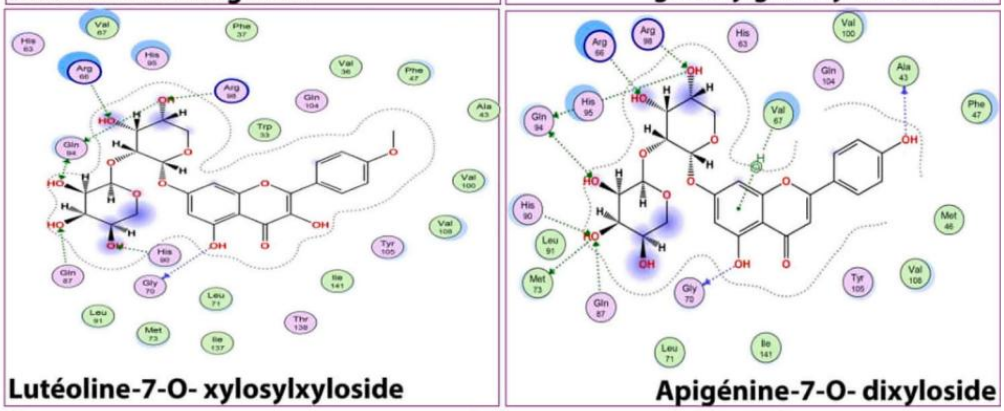
Lutéoline-7-O- xylosylxyloside
Apigénine-7-O- dixyloside

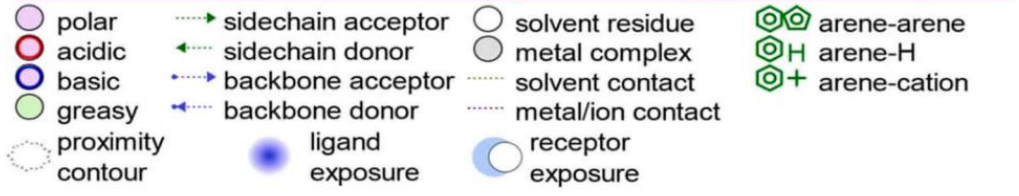
polar
acidic
basic
greasy
proximity contour
sidechain acceptor
sidechain donor
backbone acceptor
backbone donor
ligand exposure
solvent residue
metal complex
solvent contact
metal/ion contact
receptor exposure
arene-arene
arene-H
arene-cation

(caption on next page)

Fig. 4. Binding interactions of C_3, C_11, and C_12 with deoxygenated hemoglobin (PDB ID: 3WCU). (A) 3D docking poses showing the main ligand–residue interactions within the binding cavity. Hydrogen bonds are indicated by black dashed lines. (B) 2D interaction diagrams detailing hydrogen bonds, polar and hydrophobic contacts, backbone and side-chain donor/acceptor interactions, and aromatic contacts. The interaction profiles reveal the consistent involvement of key residues—including Arg98, His63, His90, His95, Gln87, and Trp33—which contribute to the stabilization of the ligand–protein complexes and may underlie their potential pharmacological relevance.

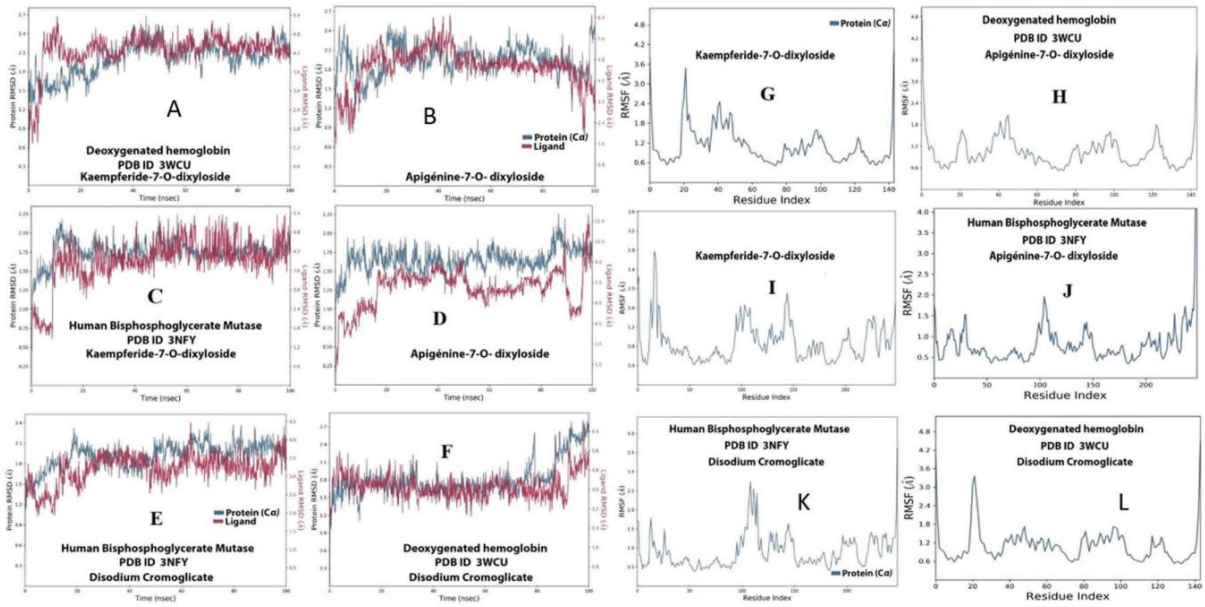

Fig. 5. A–F: Root Mean Square Deviation (RMSD) trajectories over 100 ns for protein–ligand complexes. The X-axis represents simulation time in nanoseconds (ns); the left Y-axis shows protein RMSD values in Å, while the right Y-axis shows ligand RMSD values in Å. These plots illustrate the conformational stability of disodium cromoglicate, apigenin-7-O-dixyloside, and kaempferide-7-O-dixyloside bound to deoxyhemoglobin (PDB ID: 3WCU) and human bisphosphoglycerate mutase (PDB ID: 3NFY). G–L: Root Mean Square Fluctuation (RMSF) profiles for the same protein–ligand complexes over 100 ns. The X-axis represents the protein residue index, and the Y-axis represents RMSF values in Å. These plots indicate the flexibility of individual residues within the proteins and highlight regions of higher mobility during the simulation.

3.6.1. Analysis of the stability profile by RMSD

Root mean square deviation (RMSD) provides an estimate of the structural stability of a protein-ligand complex over the course of a simulation trajectory. Compounds selected for their favorable binding to the active sites of human biphosphoglycerate mutase (PDB ID 3NFY) and deoxyhemoglobin (PDB ID 3WCU) were subjected to 100 ns molecular dynamics simulations.

For the C_11–3WCU complex, the Ca-RMSD stabilized within approximately 20 ns and remained in equilibrium throughout the simulation, reaching a final value of 4.2 Å (Fig. 5A). Similarly, the Ca-RMSD of the C_11–3NFY complex reached stability around 9 ns and maintained equilibrium with RMSD values of 5.4 Å until the end of the simulation (Fig. 5C).

In contrast, the C_12–3WCU complex exhibited initial fluctuations before stabilizing around 50 ns; equilibrium was maintained until 90 ns with RMSD values of approximately 4.8 Å, followed by minor fluctuations until the end of the simulation (Fig. 5B). The RMSD of the C_12–3NFY complex initially fluctuated, reaching

9 Å at 20 ns, stabilized until 40 ns, and then settled at 7.5 Å until 80 ns, after which the complex exhibited increased instability (Fig. 5D).

The Ca-RMSD of the C_1–3WCU complex remained stable around 4.0 Å until 90 ns, followed by minor fluctuations between 1.2 and 2.7 Å during the final 10 ns. Finally, the C_1–3NFY complex displayed greater instability relative to the other compounds, with multiple time points showing deviations from equilibrium (Fig. 5E).

For the protein (left Y-axis), RMSD analysis indicates whether the simulation has equilibrated, with fluctuations stabilizing around an average thermal structure by the end of the trajectory.

For the ligand (right Y-axis), RMSD reflects its stability relative to the protein and its binding pocket. In this study, within the 1–260 ns simulation window, the protein exhibited conformational changes exceeding 3 Å, indicating notable structural rearrangements [29]. RMSD analysis for the protein (left Y-axis) provides insight into whether the simulation has reached equilibrium, with fluctuations stabilizing around a thermal average structure toward the end of the trajectory.

As long as the overall trajectory remains stable over time, a slightly larger 3 RMSD value can still be recognized in molecular dynamics simulations, as long as it does not present continuous upward movement and converges to a stable plateau. In fact, changes between 2 and 4 are often observed in many protein-ligand complexes, especially in large or flexible proteins. These deviations usually reflect local structural adjustments rather than the dissolution of ligands [31,32].

3.6.2. Stability profile analysis by RMSF

Approximately 250 residues of 3NFY and 140 residues of 3WCU were analyzed using RMSF to assess the flexibility and fluctuation of each residue during the simulation period. For all complexes, RMSF values remained below 4.0 Å (Fig. 5). In the C_11–3WCU complex, the protein reached a maximum RMSD of 2.6 Å at 95 ns before gradually stabilizing, with RMSF values remaining below 3.6 Å until the end of the simulation (Fig. 5G). For C_11–3NFY (Fig. 5I), the maximum RMSD was 2.15 Å at 15 ns, after which the protein maintained equilibrium, and RMSF values did not exceed 2.8 Å throughout. In the C_12–3WCU complex (Fig. 5H), RMSF values were consistently below 2.4 Å, with an average

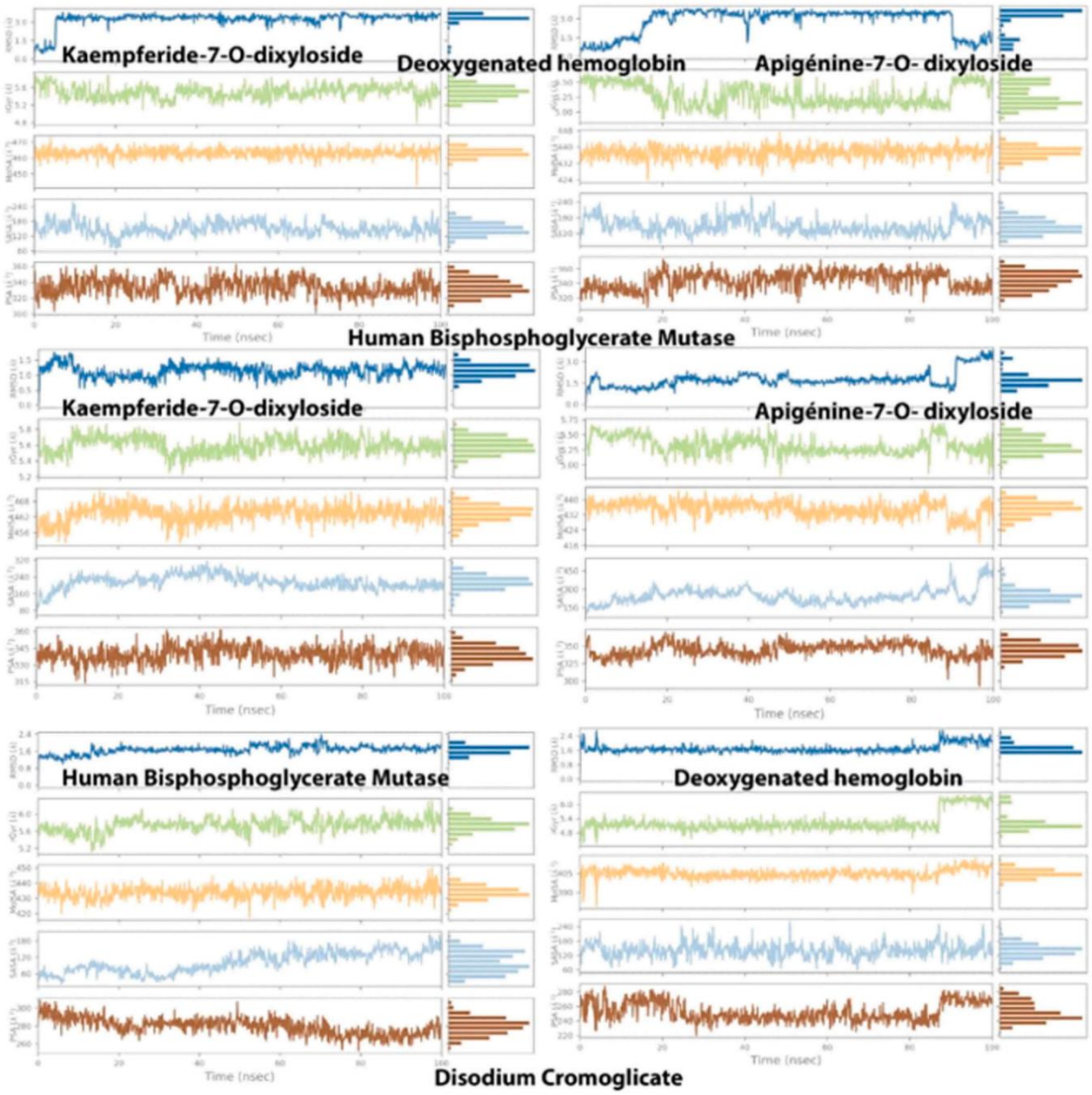

Fig. 6. Molecular dynamics trajectories over 100 ns for compounds C_1, C_11, and C_12 in complex with deoxyhemoglobin (PDB ID: 3WCU) and human bisphosphoglycerate mutase (PDB ID: 3NFY). The plots include (A) RMSD (Root Mean Square Deviation) for protein and ligand, indicating overall structural stability; (B) MolSA (Molecular Surface Area), showing changes in the molecular surface of the ligands; (C) SASA (Solvent Accessible Surface Area), representing ligand exposure to solvent; (D) rGyr (Radius of Gyration), indicating compactness of the ligands; and (E) PSA (Polar Surface Area), reflecting polar interactions. Equilibrium values are highlighted to illustrate the stabilization of the complexes throughout the simulation.

equilibrium RMSD of 2.1 Å. For the C_12–3NFY complex (Fig. 5J), maximum RMSD and RMSF values of 2.25 Å and 2.0 Å, respectively, were observed. Finally, for the C_1–3WCU and C_1–3NFY complexes (Fig. 5K,L), the protein exhibited maximum RMSD values of 2.7 Å and 2.3 Å, respectively, while RMSF remained below 3.5 Å and 2.75 Å. These results are consistent with the expected deviations of 1–3 Å for small globular proteins [28], indicating stable protein-ligand interactions throughout the simulation.

3.6.3. Ligand properties

Five ligand properties were analyzed to evaluate the stability of the

selected compounds throughout the 100 ns simulation, including ligand RMSD, molecular surface area (MolSA), solvent-accessible surface area (SASA), radius of gyration (rGyr), and polar surface area (PSA) (Fig. 6). For RMSD, the C_11–3WCU complex initially fluctuated up to 5 ns before gradually reaching equilibrium, with minor fluctuations around 82 ns, after which a new equilibrium was established. The C_12–3WCU complex stabilized within the first 20 ns, experienced minor fluctuations until 90 ns, and then re-established equilibrium until the end. The C_1–3WCU complex fluctuated during the first 9 ns and again between 80–85 ns, before gradually reaching equilibrium. RMSD values ranged from ~1.0–3.0 Å for C_11–3WCU (equilibrium at ~3 Å), ~1.1–3.1 Å for

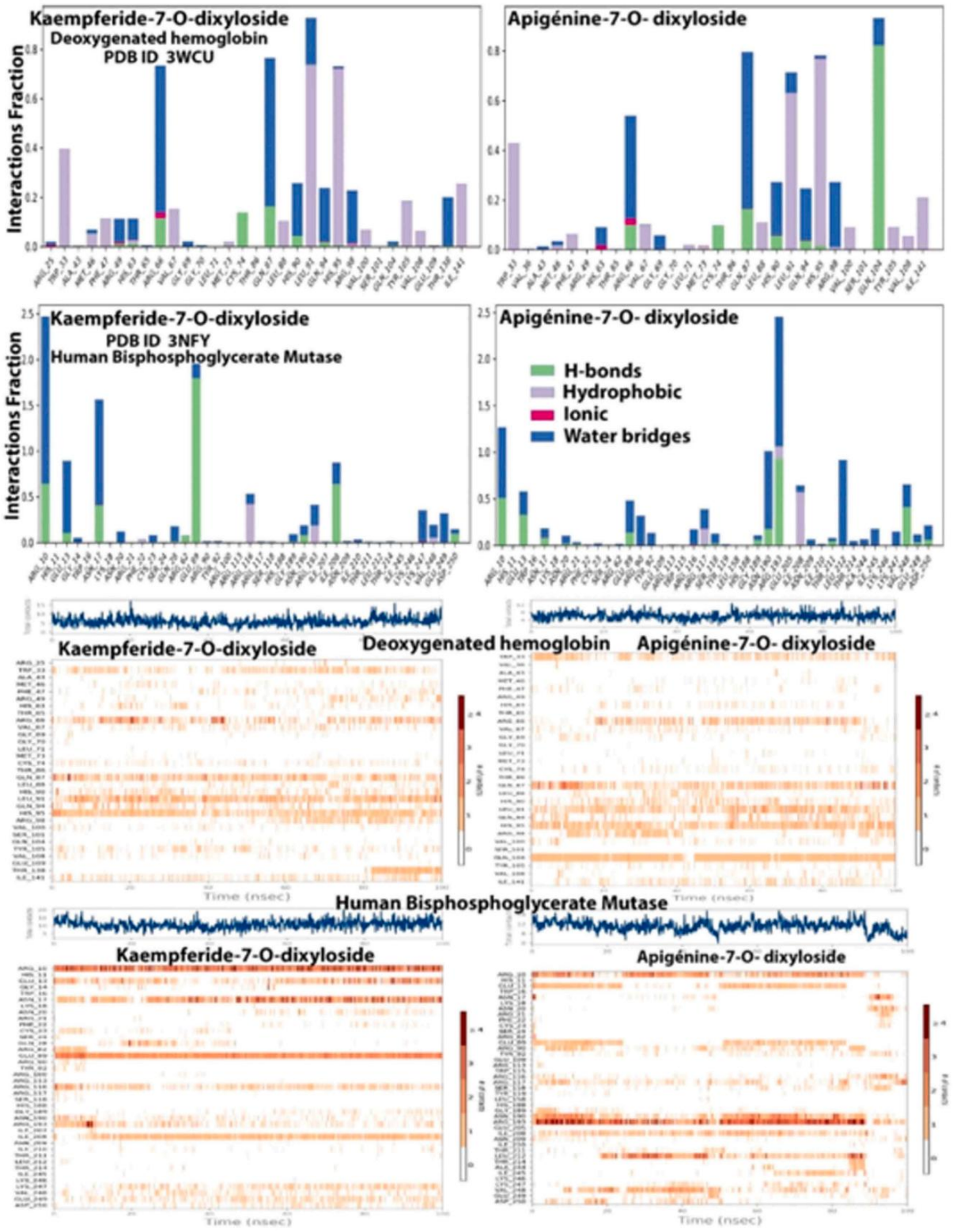

Fig. 7a. Contact plots for C_11 and C_12 with 3WCU and 3NFY, detailing hydrophobic, ionic, and hydrogen bonds (Tables 5–7) with residue labels.

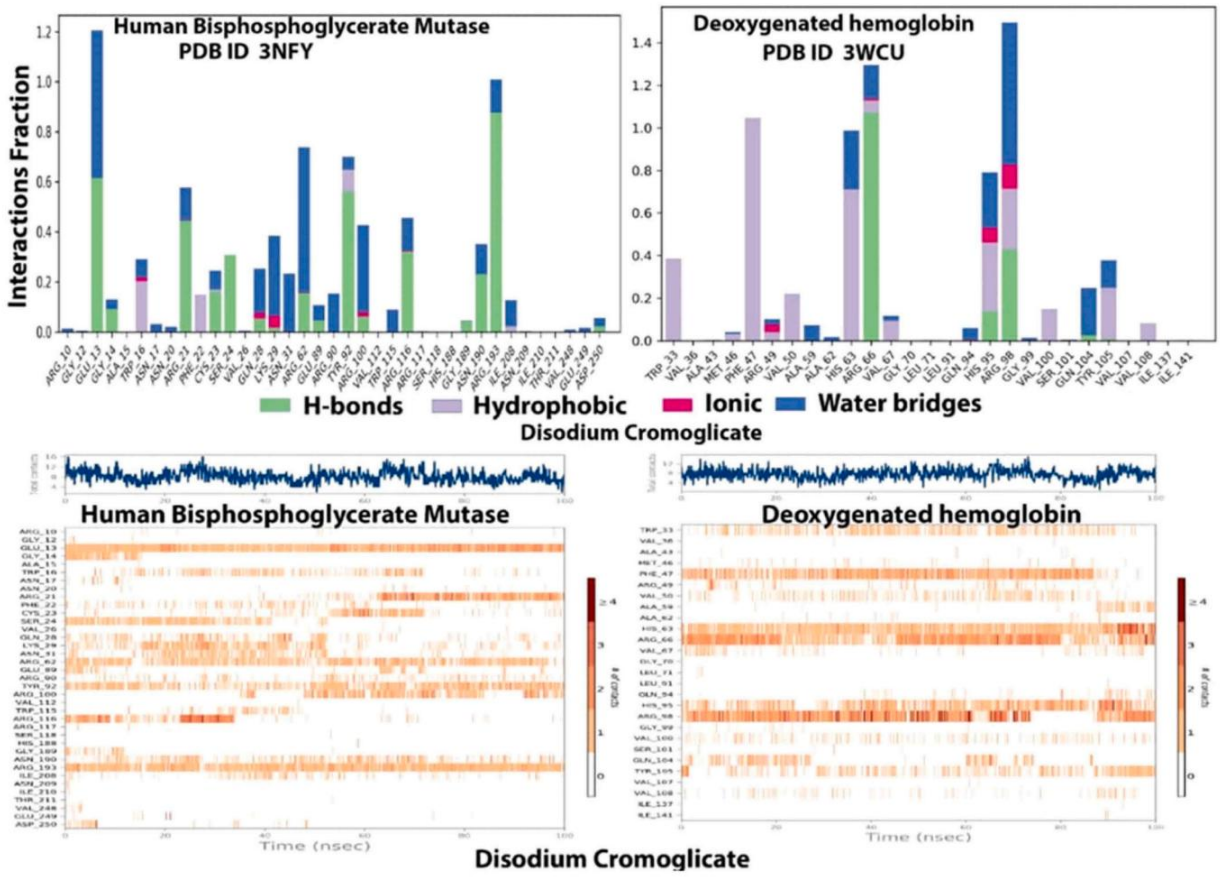

Fig. 7b. Contact plots for C_1 with 3WCU and 3NFY, including specific interactions (e.g., ARG_66, GLU_13) from Tables 5–7.

Table 5 Amino acids that interact through hydrogen bonds.

Complex	Amino acids involved in interactions
C_1–3WCU	ARG_66, HIS_95, ARG_98, GLN_104
C_11–3WCU	ARG_49, ARG_66, VAL_67, CYS_74, GLN_87, HIS_90, GLN_94
C_12–3WCU	ARG_66, CYS_74, GLN_87, HIS_90, GLN_94, HIS_95, ARG_98, GLN_104
C_1–3NFY	GLU_13, TRP_16, ASN_17, ASN_20, ARG_21, CYS_23, SER_24, GLN_28, LYS_29, ARG_62, GLU_89, TYR_92, ASL_100, ARG_116, SER_118, GLY_189, ASN_190, ARG_193, ILE_208, ASP_250
C_11–3NFY	ARG_10, GLU_13, ARG_62, GLU_89, ASN_190, ILE_208, ASP_250
C_12–3NFY)	ARG_10, GLU_13, ASN_17, ASN_20, ARG_21, GLU_89, SER_118, ASN_190, ARG_193, THR_211,VAL_248, GLU_249, ASP_250

Table 6 Amino acids that interact through ionic bonds.

Complex	Amino acids involved in interactions
C_1–3NFY	TPR_16, GLN_28, LYS_29, ARG_100
C_1–3WCU	ARG_49, HIST_95, ARG_98
C_11–3WCU	ARG_49, ARG_66

Complex	Amino acids involved in interactions
C_12–3WCU	HIST_66, ARG_66

C_12–3WCU (equilibrium at ~3 Å), and ~1.6–3.2 Å for C_1–3WCU (equilibria at ~1.6 and 2.4 Å). For the interaction with 3NFY, RMSD fluctuations were observed up to 15 ns for C_11–3NFY, followed by stable equilibrium. C_1–3NFY exhibited three equilibrium zones

Table 7 Amino acids that interact through water bonds.

Complex	Amino acids involved in interactions
C_11–3WCU	ARG_25, MET_46, ARG_49, HIS_63, ARG_66, GLY_69, GLN_87, HIS_90, LEU_91, GLN_94, HIS_95, ARG _98, GLN_104, THR_138
C_12–3WCU	ALA_43, MET_46, HIS_63, ARG_66, GLY_69, GLN_87, HIS_90, LEU_91, GLN_94, HIS_95, ARG_98, GLN_104
C_1–3WCU	MET_46, ARG_49, ALA_62, HIS_63, ARG_66, VAL_67, GLN_94, HIS_95, ARG_98, GLY_99, GLN_104, TYR_105
C_11–3NFY	ARG_10, GLU_13, GLU_14, ASN_17, ASN_20, ARG_21, CYS_23, GLN_28, LYS_29, ASN_31, ARG_62, GLU_89, ARG_90, TYR_92, ARG_100, TRP_115, ARG_116, GLY_189, ASN_190, ARG _193, ILE_208, ASN_209, ILE_210, LYS_247, VAL_248, GLU_249, ASP_250
C_1–3NFY	ARG_10, GLU_13, ASN_17, ASN_20, ARG_21, CYS_23, SER_24, ARG_62, GLU_89, ARG_90, TYR_92, ARG_116, ARG_117, ASN_190, ARG _193, ILE_208, VAL_248, GLU_249, ASP_250
C_11–3NFY	ARG_10, GLU_13, TRP_16, ASN_17, ASN_20, CYS_23, GLN_28, GLU_89, ARG_116, GLY_189, ASN_190, ARG _193, ILE_208, ASN_209, ILE_210, LYS_247, VAL_248, GLU_249, ASP_250
C_12–3NFY	ARG_10, GLU_13, ASN_17, ASN_20, ARG_21, CYS_23, SER_24, ARG_62, GLU_89, ARG_90, TYR_92, ARG_116, ARG_117, SER_118, GLY_189, ASN_190, ARG _193, ILE_208, ASN_209, THR_211, LEU_212, THR_214, ALA_244, ILE_245, LYS_246, VAL_248, GLU_249, ASP_250

between 0–15 ns, 20–53 ns, and 70–100 ns. C_12–3NFY also displayed three equilibrium zones between 5–83 ns, 85–90 ns, and 91–100 ns. RMSD values fluctuated between 1.0–2.0 Å with equilibrium around 1.1 Å for C_11–3NFY, 1.0–3.0 Å with equilibria at ~1.5, 1.0, and 3.0 Å for C_12–3NFY, and 1.2–2.4 Å with equilibria at ~1.2, 2.0, and 1.3 Å for

Table 8 Receptor-ligand interaction showing deep bands.

Complex	Amino acids involved in interactions
C_11–3WCU	TRP_33, PHE_47, HIS_63, ARG_66, HIS_95, ARG_98
C_11–3WCU	TRP_33, ARG_66; GLU_87; LEU_91; HIS_95
C_11–3WCU	TRP_33, GLU_87; LEU_91; HIS_95, GLN_104
C_1–3NFY	GLU_13, ARG_62, TYR_92, ASN_190, ARG_193
C_11–3NFY	ARG_10, ASN_17, GLU_89, ILE_208
C_12–3NFY	ARG_10, GLU_13, ASN_190, ARG_193, ILE_208

C_1–3NFY. The radius of gyration (rGyr) showed slight fluctuations before reaching equilibrium. For 3WCU interactions, rGyr values ranged from ~4.4–6.0 Å (C_1, equilibrium at 5.4–6.0 Å), ~4.8–6.2 Å (C_11, equilibrium at 5.6 Å), and ~4.75–5.75 Å (C_12, equilibrium at 5.0 Å). For 3NFY, rGyr values were ~5.0–6.0 Å (C_1, equilibrium at 5.6 Å), ~5.2–6.0 Å (C_11, equilibrium at 5.6 Å), and ~4.75–5.75 Å (C_12, equilibrium

at 5.25 Å). MolSA values fluctuated slightly during interactions with 3WCU, ranging from ~370–410 Ų with equilibrium at 405 Ų (C_1), ~440–470 Ų with equilibrium at 460 Ų (C_11), and ~424–448 Ų with equilibrium at 440 Ų (C_12). SASA values for interactions with 3WCU ranged from 60 to 240 Ų, reaching equilibrium at 120–180 Ų (C_1), 180 Ų (C_11), and 150 Ų (C_12). For 3NFY, SASA fluctuated between 30–180 Ų (C_1, equilibrium ~120 Ų), 80–240 Ų (C_11, equilibrium ~240 Ų), and 150–480 Ų (C_12, equilibrium ~150 Ų).

Polar surface area (PSA) remained mostly constant, with minor fluctuations. For 3NFY, PSA values ranged from ~250–350 Ų (C_1, equilibrium ~280 Ų), ~315–360 Ų (C_11, equilibrium ~350 Ų), and ~330–470 Ų (C_12, equilibrium ~325 Ų). For 3WCU, PSA increased from ~220–280 Ų for C_1, with equilibria at 250 Ų (30–88 ns) and 280 Ų (90–100 ns), while C_11 and C_12 fluctuated between ~300–380 Ų, reaching equilibrium at 340 Ų and 350 Ų, respectively. Overall, these analyses demonstrate that despite initial minor fluctuations, all ligands gradually reached stable equilibria in the active sites of both proteins, confirming their structural stability throughout the simulation [28].

3.6.4. Protein-ligand contacts

The contact histograms (Figs. 7a and 7b) were analyzed to characterize the protein-ligand (P-L) interactions within the stable complexes and to provide a comprehensive understanding of the molecular dynamics simulations. The P-L interactions were categorized into four types: hydrophobic interactions, ionic interactions, hydrogen bonds (including bridging), and water-mediated hydrogen bonds.

Overall, approximately 300 amino acid residues from each protein (3WCU and 3NFY) participated in these interactions, forming specific contacts through hydrophobic forces, ionic bonds, hydrogen bonds, and water bridges (Tables 5–7). Among these, hydrogen bonds are particularly critical, as they not only contribute significantly to ligand binding but also play essential roles in protein folding and stability. These interactions are therefore fundamental considerations in rational drug design and the evaluation of potential antisickling agents [28,30].

Hydrogen bonds

Ionic bonds

Water bonds

The contribution of amino acids was analyzed from the P-L interaction in each pathway. The receptor-ligand complex showed deep bands (Table 8), suggesting that these amino acid residues had more interactions with the ligands in all possible orientations [33,34].

Docking and molecular dynamics simulations indicate that the interactions between the tested compounds and the selected targets are stable, suggesting a potential inhibition of HbS polymerization in sickle cells by the two Congolese medicinal plants, *Justicia secunda* and *Moringa oleifera*.

3.7. Predictions of pharmacokinetics and drug similarity

The results of the *in silico* pharmacokinetic studies of the active compounds are shown in Table 9 and Fig. 8**.**

In silico pharmacokinetic analyses play a central role in the early stages of drug discovery by predicting a compound's absorption, distribution, metabolism, and excretion (ADME) properties from its molecular structure [28,35,36]. In this study, the pharmacokinetic and toxicity profiles of the selected compounds were assessed (Fig. 8 and Table 9). Several molecules violated Lipinski's Rule of Five (Ro5) [37], mainly due to molecular weight > 500 g/mol and an excess of hydrogen bond donors or acceptors (with C_1 having only one hydrogen bond donor). Nonetheless, all compounds exhibited molar refractivity < 140 and Consensus logP < 5, values that fall within acceptable ranges [30]. It is also important to note that Ro5 is not absolute: approximately 16 % of orally administered drugs fail at least one criterion, and 6 % fail two or more [38].

The Veber (GSK) filter considers compounds drug-like when they possess ≤ 10 rotatable bonds, a TPSA ≤ 140 Ų, and no more than 12 hydrogen bond donors and acceptors [40]. Here, all compounds showed TPSA > 140 Ų and ≥ 12 rotatable bonds. Solubility predictions using the ESOL and Ali models [36] indicated that all compounds are soluble but poorly absorbed in the gastrointestinal tract, with the exception of C_1, which showed moderate solubility; the SILICOS-IT model classified C_1 as poorly soluble.

Synthetic accessibility (SA) scores ranged from 3.8 to 7.4. Given that SA values span from 1 (easy synthesis) to 10 (difficult synthesis), compounds with scores < 6 are generally viewed as synthetically feasible, whereas higher scores may require more elaborate synthetic routes [40]. In this study, flavonoids were considered lead scaffolds intended for subsequent chemical optimization. Although certain molecules, such as C_3 (7.42), show elevated SA values, the leading candidates C_11 (6.15) and C_12 (5.92) remain within a moderately accessible range, which is acceptable for natural product-derived leads. These synthetic challenges can be addressed through targeted functionalization, semi-synthetic strategies, or analog development, supporting the practical adaptability of these scaffolds rather than suggesting inherently simple synthesis.

With regard to drug metabolism, nearly all compounds were predicted to be P-glycoprotein (P-gp) substrates except C_2, and most were predicted to be non-inhibitors of the major CYP450 isoenzymes (CYP1A2, CYP2C9, CYP2C19, CYP2D6, and CYP3A4), except for C_1. All compounds exhibited low skin permeability (Log Kp), indicating limited transdermal absorption [39]. Despite these pharmacokinetic constraints, flavonoids continue to attract interest due to their documented biological activity and the possibility of improving their performance through formulation technologies or chemical modification. Prior studies have reported experimentally validated antisickling activity for flavonoids such as quercetin, kaempferol, and naringenin, which inhibit HbS polymerization and improve red blood cell morphology in vitro [41, 42].

Taken together, the evaluated compounds generally meet key pharmacokinetic criteria and exhibit drug-like behavior, even if some parameters fall outside ideal ranges [43,44].

4. Conclusion

Across African populations, sickle cell disease (SCD) remains a major public health concern. Molecules derived from plants that have the ability to enter red blood cells, stabilize hemoglobin S, or interfere with the formation of tactoids are frequently considered initial targets for antisickling research. Thirteen components from Justicia secunda and Moringa oleifera were molecularly docked in this work, and the results consistently showed negative binding energies with deoxyhemoglobin and/or human biphosphoglycerate mutase, indicating the formation of thermodynamically stable complexes *in silico*.

Table 9 ADMET profile of the active compounds.

Parameters	Compound number				
	1	3	9	11	12
Physicochemical Properties					
Formula	C_23H14Na2O11	C_33H40O19	C_25H26O14	C_26H28O14	C_25H26O13
Molecular weight (g/mol)	512.33	740.66	550.47	564.49	534.47
Num. heavy atoms	36	52	39	40	38
Num. arom. heavy atoms	20	16	16	16	16

Parameters	Compound number				
Fraction Csp3	0.13	0.55	0.40	0.42	0.40
Num. rotatable bonds	10	9	5	6	5
Num. H-bond acceptors	11	19	14	14	13
Num. H-bond donors	1	11	8	7	7
Molar Refractivity	112.64	169.72	128.58	133.05	126.56
TPSA (Ų)	151.71	308.12	228.97	217.97	208.74
Lipophilicity					
Log Po/w (iLOGP)	0.00	1.53	2.33	1.99	2.50
Log Po/w (XLOGP3)	2.28	-1.98	-0.74	-0.42	-0.25
Log Po/w (WLOGP)	1.96	-3.27	-1.14	-0.84	-0.85
Log Po/w (MLOGP)	-0.84	-5.04	-3.09	-2.89	-2.62
Log Po/w (SILICOS IT)	0.62	-3.28	-1.27	-0.72	-0.80
Consensus Log Po/w	0.80	-2.41	-0.78	-0.58	-0.40
Water Solubility					
Log S (ESOL)	-4.20	-2.82	-2.76	-2.98	-2.98
Solubility (mg/mL)/ (mol/l)	3.20e-02/6.25e-05	1.13e+00/1.52e-03	9.56e-01/1.74e-03	5.98e-01/1.06e-03	5.63e-01/1.05e-03
Class	MS*	Soluble	Soluble	Soluble	Soluble
Log S (Ali)	-5.10	-3.97	-3.59	-3.69	-3.68
Solubility (mg/mL)	4.04e-03	7.99e-02	1.41e-01	1.15e-01	1.13e-01
Solubility (mol/l)	7.89e-06	1.08e-04	2.56e-04	2.03e-04	2.11e-04
Class	MS*	Soluble	Soluble	Soluble	Soluble
Log S (SILICOS-IT)	-6.44	0.35	-1.19	-1.87	-1.78
Solubility (mg/mL)/(mol/l)	1.84e-04/3.60e-07	1.68e+03/2.26e+ 00	3.60e+01/6.53e-02	7.61e+00/1.35e-02	8.89e+00/1.66e-02
Class	PS**	Soluble	Soluble	Soluble	Soluble
Pharmacokinetics					
GI absorption	Low	Low	Low	Low	Low
BBB permeant	No	No	No	No	No
P-gp substrate	Yes	No	Yes	Yes	Yes

Parameters	Compound number				
CYP1A2 inhibitor	No	No	No	No	No
CYP2C_19 inhibitor	Yes	No	No	No	No
CYP2C_9 inhibitor	Yes	No	No	No	No
CYP2D6 inhibitor	No	No	No	No	No
CYP3A4 inhibitor	Yes	No	No	No	No
Log Kp (skin permeation; cm/s	-7.81	-12.22	-10.18	-10.04	-9.74
Druglikeness					
Lipinski	No; 2 violations: MW>500, NorO>10	No; 3 violations: MW>500, NorO>10, NHorOH>5	No; 3 violations: MW>500, NorO>10, NHorOH>5	No; 3 violations: MW>500, NorO>10, NHorOH>5	No; 3 violations: MW>500, NorO>10, NHorOH>5
Ghose	No; 1 violation: MW>480	No; 4 violations: MW>480, WLOGP<-0.4, MR>130, #atoms>70	No; 2 violations: MW>480, WLOGP<-0.4	No; 3 violations: MW>480, WLOGP<-0.4, MR>130	No; 2 violations: MW>480, WLOGP<-0.4
Veber	No; 1 viola-tion:TPSA>140	No; 1 violation: TPSA>140	No; 1 violation: TPSA>140	No; 1 violation: TPSA>140	No; 1 violation: TPSA>140
Egan	No; 1 violation: TPSA>131.6	No; 1 violation: TPSA>131.6	No; 1 violation: TPSA>131.6	No; 1 violation: TPSA>131.6	No; 1 violation: TPSA>131.6
Muegge	No; 2 violations: TPSA>150, H-acc>10	No; 4 violations: MW>600, TPSA>150, H-acc>10, H-don>5	No; 3 violations: TPSA>150, H-acc>10, H don>5	No; 3 violations: TPSA>150, H-acc>10, H don>5	No; 3 violations: TPSA>150, H-acc>10, H don>5
Bioavailability Score	0.17	0.17	0.17	0.17	0.17
Medicinal Chemistry					
PAINS	0 alert	0 alert	1 alert: catechol_A	0 alert	0 alert
Brenk	0 alert	0 alert	1 alert: catechol	0 alert	0 alert

Parameters	Compound number				
Leadlikeness	No; 2 violations: MW>350, Rotors>7	No; 2 violations: MW>350, Rotors>7	No; 1 violation: MW>350	No; 1 violation: MW>350	No; 1 violation: MW>350
Synthetic	3.82	7.42	5.97	6.15	5.92

* Moderately soluble, ** Poorly soluble

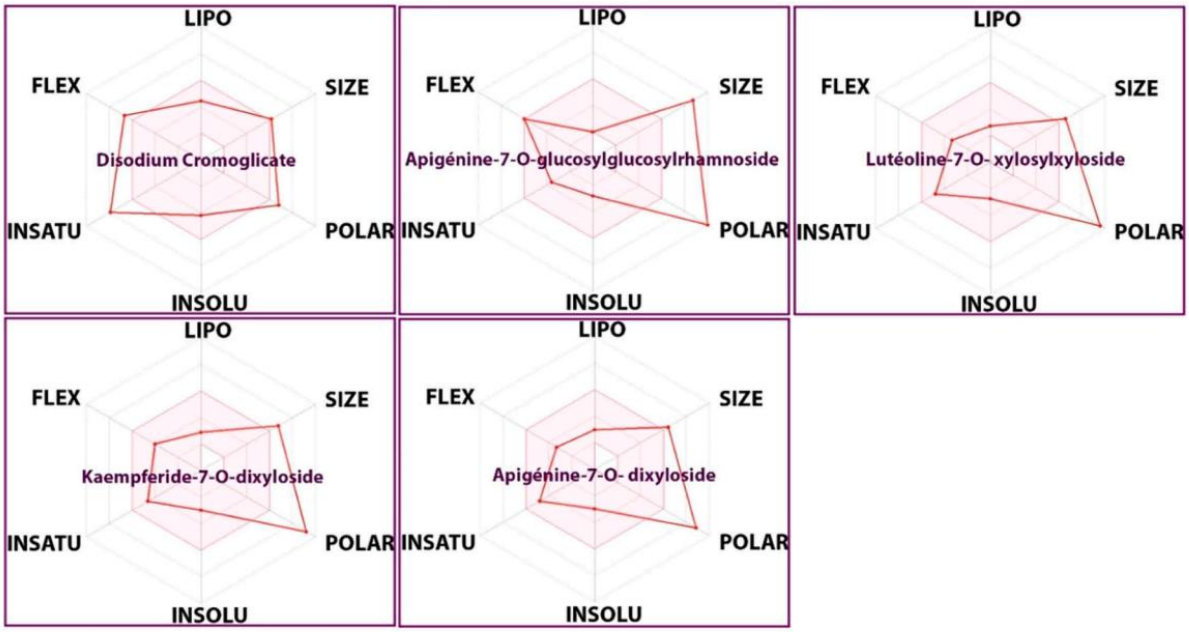

Fig. 8. ADMET profiles (Table 9) for C_1, C_3, C_9, C_11, and C_12. Each ligand within the pink area of the radar chart indicates an ADME profile that is acceptable according to Lipinski's rule of five (Ro5), which includes size, lipophilicity (LogP) and polarity (TPSA), flexibility (the number of hydrogen bond donors and acceptors).

These computational results highlight C_11 and C_12 as significant *in silico* leads or structural scaffolds that warrant further investigation and provide a scientific justification for the traditional use of these plants. However, these findings should not be seen as proof of therapeutic efficacy. They merely draw attention to molecular interactions that support further experimental analysis. Before any claim about their potential as drug candidates can be made responsibly, thorough *in vitro* and *in vivo* research is necessary, followed by optimization to evaluate pharmacokinetic behavior, pharmacodynamic responses, and safety.

Preparations from these species are already used in Congolese traditional medicine to help people with sickle cell disease with symptoms like fatigue, painful crises, and anemia. These practices are supported scientifically by the demonstration of plausible molecular interactions, but empirical validation is still required. Instead, it shows how indigenous pharmacopoeias can guide early research efforts to create accessible and culturally grounded approaches to managing sickle cell disease, as long as later laboratory and clinical data validate their usefulness.

Author contributions: CRediT

Gbolo B.Z. conducted the biological experiments, analyzed the data and wrote the original draft. Ngbolua K.N. Wrote, reviewed and edited Methodology. Semay I. and Gerbaux P. carried out the chemical analysis. Wafa Ali Eltayb, Samah Shabana, Hamed I. Hamouda, Mohamed Mohsen and Xiling Wang carried out the *in silico* analysis; Mohnad Abdalla design the *in silico* analysis and supervises it. Mulongo E.K. Wrote, reviewed and edited Data curation. Mpiana P.T., Duez P. designed the study and supervised it. All authors read and approved the final manuscript.

CRediT authorship contribution statement

Mulongo Emmanuel K.: Writing – review & editing, Software, Formal analysis, Data curation. **Wafa Ali Eltayb:** Writing – review & editing, Software, Formal analysis. **Mohnad Abdalla:** Writing – review & editing, Supervision, Software, Investigation, Formal analysis, Data curation. **Gbolo Zoawe Benjamin:** Writing – original draft. **Samah Shabana:** Writing – review & editing, Software, Formal analysis. **Ngbolua K. N.:** Writing – review & editing, Methodology, Data curation. **Irene ' Semay:** Writing – review & editing, Software, Formal analysis, Data curation. **P. Gerbaux:** Writing – review & editing, Supervision, Investigation, Data curation. **Hamed I. Hamouda:** Writing – review & editing, Visualization, Software, Formal analysis. **Pius T. Mpiana:** Writing – review & editing, Validation, Supervision, Project administration, Conceptualization. **Mohamed Mohsen:** Writing – review & editing, Software, Formal analysis. **Pierre Duez:** Writing – review & editing, Validation, Supervision, Project administration, Investigation, Funding acquisition, Conceptualization. **Xiling Wang:** Writing – review & editing, Software, Formal analysis, Data curation.

Funding

This project was carried out thanks to funding of the Academy of Research and Higher Education (ARES), Grant number: COOP-CONV-18–004, AI ARES UNIKIN, of which Mr. Gbolo was the main beneficiary.

Declaration of Competing Interest

The authors declare that they have no known competing financial interests or personal relationships that could have appeared to influence the work reported in this paper.

Acknowledgements

The authors would like to thank Mr Claudio Palmieri for his assistance and collaboration.

Appendix A. Supporting information

Supplementary data associated with this article can be found in the online version at doi:10.1016/j.prenap.2026.100516.

Data availability

No data was used for the research described in the article.

References

- [1] C.K. Tebbi, Sickle cell disease, a review, Hemato 3 (2022) 341–366, https://doi. org/10.3390/hemato3020024.

- [2] C. Elendu, et al., Understanding sickle cell disease causes, symptoms, and treatment options, Med. (Baltim.) 102 (38) (2023) 1–7, https://doi.org/10.1097/ MD.0000000000035237.
- [3] K.M. Knee, et al., Sickle cell disease model mice lacking 2,3-Dpg show reduced RBC sickling and improvements in markers of hemolytic anemia, Blood 136 (ement 1) (2020) 27–28, https://doi.org/10.1182/blood-2020-142052.
- [4] B.Z. Gbolo, et al., In Vitro Biological Activities of Drepanoalpha ® Ethanolic Extract, A Justicia secunda and Moringa oleifera -Based Phytomedicine Proposed for The Symptomatic Treatment of Sickle Cell Disease, J. Fundam. Appl. Pharm. Sci. 3 (2) (2023) 64–82, https://doi.org/10.18196/jfaps.v2i1.16000.
- [5] D. Alramadhani, A.S. Aljahdali, O. Abdulmalik, B.D. Pierce, M.K. Safo, Metabolic reprogramming in sickle cell diseases: pathophysiology and drug discovery opportunities, Int. J. Mol. Sci. 23 (7448) (2022) 1–19.
- [6] M.J. Telen, P. Malik, G.M. Vercellotti, Therapeutic strategies for sickle cell disease: towards a multi-agent approach, Nat. Rev. Drug Discov. 18 (2) (2019) 139–158, https://doi.org/10.1038/s41573-018-0003-2.
- [7] O.O. Olubiyi, M.O. Olagunju, B. Strodel, Rational drug design of peptide-based therapies for sickle cell disease, Molecules 24 (24) (2019) 1–23, https://doi.org/ 10.3390/molecules24244551.
- [8] F.O. Ohiagu, P.C. Chikezie, C.M. Chikezie, Sickle hemoglobin polymerization and antisickling medicinal plants, J. Phytopharm. 10 (2) (2021) 126–133, https://doi. org/10.31254/phyto.2021.10209.
- [9] E.R. Henry, et al., Allosteric control of hemoglobin S fiber formation by oxygen and its relation to the pathophysiology of sickle cell disease, Proc. Natl. Acad. Sci. U. S. A. 117 (26) (2020) 15018–15027, https://doi.org/10.1073/pnas.1922004117.
- [10] W.A. Eaton, Hemoglobin S polymerization and sickle cell disease: a retrospective on the occasion of the 70th anniversary of Pauling's Science paper, Am. J. Hematol. 95 (2) (2019) 205–211, https://doi.org/10.1002/ajh.25687.
- [11] P.G. Gallagher, Disorders of erythrocyte hydration, Blood 130 (25) (2017) 2699–2708, https://doi.org/10.1182/blood-2017-04-590810.
- [12] C. Brugnara, Sickle cell dehydration: pathophysiology and therapeutic applications, Clin. Hemorheol. Micro 68 (2–3) (2018) 187–204, https://doi.org/ 10.3233/CH-189007.
- [13] F.B. Piel, M.H. Steinberg, D.C. Rees, Sickle cell disease, N. Engl. J. Med. 376 (16) (2017) 1561–1573, https://doi.org/10.1056/NEJMra1510865.
- [14] P.H. Chow, et al., Inhibition of the Aquaporin-1 Cation Conductance by Selected Furan Compounds Reduces Red Blood Cell Sickling, Front. Pharm. 12 (January) (2022) 1–13, https://doi.org/10.3389/fphar.2021.794791.
- [15] T. Kassa, F. Wood, M.Brad Strader, A.I. Alayash, Antisickling drugs targeting βCys93 reduce iron oxidation and oxidative changes in sickle cell hemoglobin, Front. Physiol. 10 (JUL) (2019), https://doi.org/10.3389/fphys.2019.00931.
- [16] W.A. Eaton, Impact of hemoglobin biophysical studies on molecular pathogenesis and drug therapy for sickle cell disease, Mol. Asp. Med. 84 (2022) (2022) 1–10, https://doi.org/10.1016/j.mam.2021.100971.
- [17] L. Bizumukama, A. Ferster, B. Gulbis, A. Kumps, F. Cotton, In vitro inhibitory effects of disodium cromoglycate on ionic transports involved in sickle cell dehydration, Pharmacology 83 (5) (2009) 318–322, https://doi.org/10.1159/ 000215598.
- [18] J. Tomc, N. Debeljak, Molecular pathways involved in the development of congenital erythrocytosis, Genes (Basel) 12 (1150) (2021) 1–20, https://doi.org/ 10.3390/genes12081150.

- [19] B.Z. Gbolo, et al., LC-MS/MS Analysis of crude Flavonoid Compounds from Justicia secunda from Democratic Republic of the Congo and evaluation of their antisickling Activity, Nat. Resour. Hum. Heal 4 (4) (2024) 387–397, https://doi. org/10.53365/nrfhh/192594.
- [20] B.Z. Gbolo, et al., Profilage phytochimique par chromatographie sur couche mince haute performance d'extraits de flavonoïdes totaux du Drepanoalpha® et ´evaluation de leur activit´e anti-dr´epanocytaire in vitro, Ann. Afr. Med. 16 (1) (2022) 4882–4898, https://doi.org/10.4314/aamed.v16i1.3.
- [21] S.J. Sheela, et al., Potential impacts of solvents topological aspects, Vanderwal effect, spectral investigation, and biological features of dodecyl 3,4,5-trihydroxybenzoate: anti-viral agent, Spectrosc. Lett. 58 (7) (2025) *651–666*, https://doi.org/ 10.1080/00387010.2025.2457397.
- [22] P.T. Mpiana, et al., Identification of potential inhibitors of SARS-CoV-2 main protease from Aloe vera compounds: a molecular docking study, Chem. Phys. Lett. 754 (2020) 1–7, https://doi.org/10.1016/j.cplett.2020.137751.
- [23] A. Matondo, et al., In silico drug repurposing of anticancer drug 5-FU and analogues against SARS-CoV-2 main protease: molecular docking, pharmacokinetics and chemical reactivity, Adv. Appl. Bioinforma. Chem. 15 (8) (2022) 59–77. □https://chemrxiv.org/engage/chemrxiv/article-details/62628aa5d048edcdf94d1171□ ([Online]. Available).
- [24] M.M. Charly, et al., Molecular docking and molecular dynamics simulation studies of the interaction of anti-oral cancer plant Curcuma longa derived-compounds with human epidermal growth factor receptor 2, J. Proteins Proteom. 15 (3) (2024) 491–507, https://doi.org/10.1007/s42485-024-00158-4.
- [25] A. Emmanuel Kitete Mulongo, K.T.N. Matondo, Ngbolua, P.T. Mpiana, Evaluation of antiviral potential of Cinchona officinalis derived compounds against COVID-19 and human hepatitis B: an in silico molecular docking and molecular dynamics simulation study, Pharmacol. Res. Nat. Prod. 7 (April) (2025) 100229, https://doi. org/10.1016/j.prenap.2025.100229.
- [26] E.M. Lengbiye, et al., Antimicrobial activity and structure elucidation of Pterosterone, a naturally occurring phytoecdysteroid isolated from the leaves of Vitex madiensis Oliv. (Lamiaceae) (no), Pharmacol. Res. Nat. Prod. 7 (2025) 100264, https://doi.org/10.1016/j.prenap.2025.100264.
- [27] M. Miar, A. Shiroudi, K. Pourshamsian, A.R. Oliaey, F. Hatamjafari, Theoretical investigations on the HOMO–LUMO gap and global reactivity descriptor studies, natural bond orbital, and nucleus-independent chemical shifts analyses of 3-phenylbenzo[d]thiazole-2(3H)-imine and its para-substituted devivatives: solvent and subs, J. Chem. Res. 45 (1–2) (2021) 147–158, https://doi.org/10.1177/ 1747519820932091.
- [28] M. Abdalla, W.A. Eltayb, A.A. El-Arabey, K. Singh, X. Jiang, Molecular dynamic study of SARS-CoV-2 with various S protein mutations and their effect on thermodynamic properties, Comput. Biol. Med. 141 (2022) 1–7, https://doi.org/ 10.1016/j.compbiomed.2021.105025.
- [29] E. Kitete, J. Kilembe, N.M. Yvette, A. Matondo, K. Ngbolua, D. Dinangayi, Molecular docking, DFT and dynamics simulations of Jatropha curcas-derived compounds targeting PR and hER for Breast Cancer Treatment, Res 2 (2025) (2025) 1–18,https://doi.org/10.1016/j.nexres.2025.100249.
- [30] A. Boufissiou, et al., In-silico investigation of phenolic compounds from leaves of Phillyrea angustifolia L. as a potential inhibitor against the SARS-CoV-2 main protease (Mpro PDB ID:5R83) using a virtual screening method, J. Saudi Chem. Soc. 26 (3) (2022) 1–16, https://doi.org/10.1016/j.jscs.2022.101473.
- [31] S.A. Hollingsworth, R.O. Dror, Molecular dynamics simulation for all, Neuron 99 (6) (2018) 1129–1143, https://doi.org/10.1016/j.neuron.2018.08.011.
- [32] A. Hospital, et al., Molecular dynamics simulations: advances and applications, Adv. Appl. Bioinforma. Chem. 8 (2015) 37–47, https://doi.org/10.2147/AABC. S70333.
- [33] A. Pasquadibisceglie, F. Polticelli, Structural determinants of ligands recognition by the human mitochondrial basic amino acids transporter SLC25A29. Insights from molecular dy-

namics simulations of the c-state, Comput. Struct. Biotechnol. J. 19 (2021) 5600–5612, https://doi.org/10.1016/j.csbj.2021.10.007.

- [34] M. Abdalla, et al., In silico studies on phytochemicals to combat the emerging COVID-19 infection, J. Saudi Chem. Soc. 25 (12) (2021) 1–16, https://doi.org/ 10.1016/j.jscs.2021.101367.
- [35] S. Ekins, J. Mestres, B. Testa, In silico pharmacology for drug discovery: methods for virtual ligand screening and profiling, Br. J. Pharm. 152 (1) (2007) 9–20, https://doi.org/10.1038/sj.bjp.0707305.
- [36] J.-P. K.-T.-N. Ngbolua, et al., In silico studies on the interaction of four cytotoxic compounds with angiogenesis target protein HIF-1α and human androgen receptor and their ADMET properties, Bull. Natl. Res. Cent. 46 (101) (2022) 1–12, https:// doi.org/10.1186/s42269-022-00793-1.
- [37] L. Guan, et al., ADMET-score-a comprehensive scoring function for evaluation of chemical drug-likeness, Medchemcomm 10 (1) (2019) 148–157, https://doi.org/ 10.1039/C8MD00472B.
- [38] G.R. Bickerton, G.V. Paolini, J. Besnard, S. Muresan, A.L. Hopkins, Quantifying the chemical beauty of drugs, Nat. Chem. 4 (2) (2012) 90–98, https://doi.org/ 10.1038/nchem.1243.
- [39] D. Ranjith, C. Ravikumar, SwissADME predictions of pharmacokinetics and druglikeness properties of small molecules present in Ipomoea mauritiana Jacq, J. Pharmacogn. Phytochem 8 (5) (2019) 2063–2073. □http://www.swissadme.ch/ index.php□ ([Online]. Available).
- [40] P. Ertl, A. Schuffenhauer, Estimation of synthetic accessibility score of drug-like molecules based on molecular complexity and fragment contributions, J. Chemin.. 1 (1) (2009) 1–11, https://doi.org/10.1186/1758-2946-1-8.
- [41] M. Cesquini, M.A. Torsoni, G.R. Stoppa, S.H. Ogo, t -BOOH-induced oxidative damage in sickle red blood cells and the role of flavonoids, Biomed. Pharm. 57 (2003) 124–129, https://doi.org/10.1016/S0753-3322(03)00018-0.
- [42] O.F. Kunle, H.O. Egharevba, Chemical constituents and biological activity of medicinal plants used for the management of sickle cell disease - A review, J. Med. Plants Res. 7 (48) (2013) 3452–3476, https://doi.org/10.5897/JMPR2013.5333x.
- [43] I. Muegge, S.L. Heald, D. Brittelli, Simple selection criteria for drug-like chemical matter, J. Med. Chem. 44 (12) (2001) 1841–1846, https://doi.org/10.1021/ jm015507e.
- [44] Y.C. Martin, A bioavailability score, J. Med. Chem. 48 (9) (2005) 3164–3170, https://doi.org/10.1021/jm0492002.